












Switching of the electron-phonon interaction in  $1T$ -VSe<sub>2</sub> assisted by hot carriers

Paulina Majchrzak <sup>1,2</sup> Sahar Pakdel <sup>1</sup> Deepnarayan Biswas,<sup>1</sup> Alfred J. H. Jones <sup>1</sup> Klara Volckaert <sup>1</sup> Igor Marković <sup>3,4</sup> Federico Andreatta,<sup>1</sup> Raman Sankar,<sup>5</sup> Chris Jozwiak <sup>6</sup> Eli Rotenberg,<sup>6</sup> Aaron Bostwick,<sup>6</sup> Charlotte E. Sanders <sup>2</sup> Yu Zhang,<sup>2</sup> Gabriel Karras,<sup>2</sup> Richard T. Chapman,<sup>2</sup> Adam Wyatt,<sup>2</sup> Emma Springate <sup>2</sup> Jill A. Miwa,<sup>1</sup> Philip Hofmann,<sup>1</sup> Phil D. C. King <sup>3</sup> Nicola Lanatà <sup>1,7</sup> Young Jun Chang,<sup>8,9</sup> and Søren Ulstrup <sup>1,\*</sup>

<sup>1</sup>Department of Physics and Astronomy, Interdisciplinary Nanoscience Center, Aarhus University, 8000 Aarhus C, Denmark

<sup>2</sup>Central Laser Facility, STFC Rutherford Appleton Laboratory, Harwell OX11 0QX, United Kingdom

<sup>3</sup>SUPA, School of Physics and Astronomy, University of St Andrews, St Andrews KY16 9SS, United Kingdom

<sup>4</sup>Max Planck Institute for Chemical Physics of Solids, Nöthnitzer Straße 40, 01187 Dresden, Germany

<sup>5</sup>Institute of Physics, Academia Sinica, Taipei 11529, Taiwan, Republic of China

<sup>6</sup>Advanced Light Source, E. O. Lawrence Berkeley National Laboratory, Berkeley, California 94720, USA

<sup>7</sup>Nordita, KTH Royal Institute of Technology and Stockholm University, Roslagstullsbacken 23, 10691 Stockholm, Sweden

<sup>8</sup>Department of Physics, University of Seoul, Seoul 02504, Republic of Korea

<sup>9</sup>Department of Smart Cities, University of Seoul, Seoul, 02504, Republic of Korea



(Received 12 November 2020; revised 4 March 2021; accepted 3 June 2021; published 16 June 2021)

We apply an intense infrared laser pulse in order to perturb the electronic and vibrational states in the three-dimensional charge density wave material  $1T$ -VSe<sub>2</sub>. Ultrafast snapshots of the light-induced hot carrier dynamics and nonequilibrium quasiparticle spectral function are collected using time- and angle-resolved photoemission spectroscopy. The hot carrier temperature and time-dependent electronic self-energy are extracted from the time-dependent spectral function, revealing that incoherent electron-phonon interactions heat the lattice above the charge density wave critical temperature on a timescale of  $(200 \pm 40)$  fs. Density functional perturbation theory calculations establish that the presence of hot carriers alters the overall phonon dispersion and quenches efficient low-energy acoustic phonon scattering channels, which results in a new quasiequilibrium state that is experimentally observed.

DOI: [10.1103/PhysRevB.103.L241108](https://doi.org/10.1103/PhysRevB.103.L241108)

The metallic transition-metal dichalcogenide (TMDC)  $1T$ -VSe<sub>2</sub> exhibits a charge density wave (CDW) transition at a temperature below  $T_c = 110$  K with in-plane commensurate  $(4 \times 4)$  and out-of-plane incommensurate components [1–3], in addition to very subtle spectroscopic signatures [4]. A narrow partial gap of 24 meV has been detected by tunneling spectroscopy [5], while no replica bands around the CDW wave vector have been observed by angle-resolved photoemission (ARPES) measurements [6–8]. The CDW transition temperature and electronic gap of  $1T$ -VSe<sub>2</sub> can be substantially enhanced by reducing the thickness of the material or by applying high pressure [9–14].

An unexplored strategy of modifying the CDW phase relies upon optically exciting the material with an intense laser pulse. The ensuing dynamics reveals a hierarchy of processes, including carrier-carrier screening, electron-optical phonon coupling (EPC), and low-energy soft acoustic phonon scattering [15,16]. In particular, controlling electron-phonon interactions with ultrafast light pulses can potentially lead to dynamically enhanced EPC, which has been explored using coherently driven phonon modes [17–19]. In this work, we show that the momentum-dependent EPC in  $1T$ -VSe<sub>2</sub> is dynamically altered without coherent phonons, but by the

photoinduced evolution of the hot carrier distribution via the charge carrier screening of lattice vibrations. As  $1T$ -VSe<sub>2</sub> constitutes a clean prototypical three-dimensional (3D) CDW material unlike most other (semi)metallic TMDCs that display competing CDW, excitonic, or Mott insulator phases [20–24], we anticipate that the disentangled electron-phonon dynamics underpins CDW phase transitions in general.

We employ time-resolved ARPES (TR-ARPES) with a 1.55 eV pump pulse at a repetition rate of 1 kHz and a fluence of 2.2 mJ/cm<sup>2</sup> in order to excite electrons around the Fermi level,  $E_F$ , of  $1T$ -VSe<sub>2</sub>. The excited state is probed by photoemission using a femtosecond extreme ultraviolet (XUV) probe pulse with a photon energy of 29.6 eV after a variable time delay. The experimental time and energy resolution are 40 fs and 400 meV, respectively [25]. By tracking the relaxation of the excited state quasiparticle spectrum, it is possible to extract the hot carrier temperature and to determine the temporal evolution of the electron-phonon interaction [20–24,26,27]. Single crystals of  $1T$ -VSe<sub>2</sub> have been grown using the chemical vapor transport method with I<sub>2</sub> as a transport agent [28,29]. Unless otherwise stated, all photoemission experiments have been carried out with the sample held at a temperature of  $\approx 70$  K, ensuring that at equilibrium, the material is measured in its CDW phase.

To select a 2D ( $E_{\text{bin}}, k_{\parallel}$ )-cut of the photoemission intensity that tracks excited carriers in the dispersion around  $E_F$ ,

\*Corresponding author: [ulstrup@phys.au.dk](mailto:ulstrup@phys.au.dk)

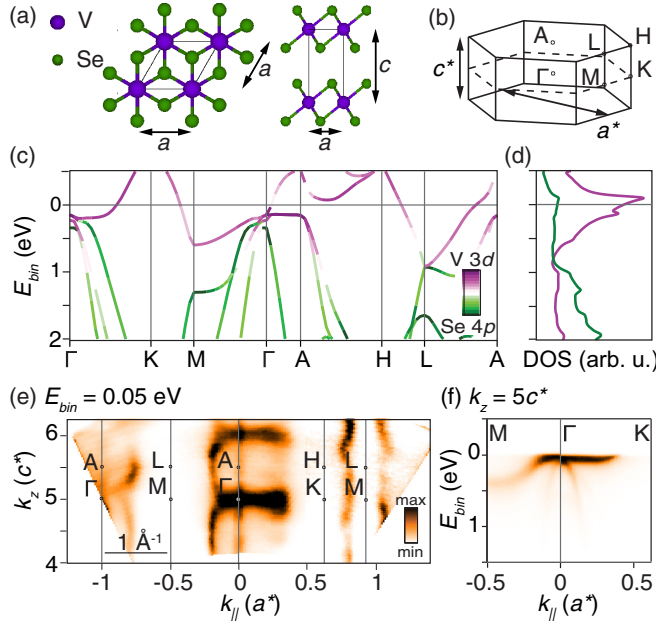


FIG. 1. (a) Crystal structure of 1T-VSe<sub>2</sub> with lattice parameters  $a$  and  $c$ . (b) Hexagonal BZ and high-symmetry points with in-plane repetition  $a^* = 4\pi/\sqrt{3}a$  and out-of-plane repetition  $c^* = 2\pi/c$ . Double-headed arrows indicate dimensions. (c) Band structure projected onto V 3d and Se 4p orbitals calculated by DFT. (d) Corresponding density of states (DOS) separated in contributions from the V 3d (purple curve) and Se 4p (green curve) orbitals. (e) Photoemission intensity for the  $(k_{\parallel}, k_{\perp})$ -plane spanning the given high-symmetry points at a binding energy of 0.05 eV. (f) ARPES cut obtained for  $k_{\perp} = 5c^*$ , corresponding to the  $M$ - $\Gamma$ - $K$  direction.

we first characterize the static photoemission properties of 1T-VSe<sub>2</sub>. In the normal state, the system adopts the tetragonal crystal structure in Fig. 1(a) with the corresponding hexagonal Brillouin zone (BZ) shown in Fig. 1(b). The electronic band structure and density of states (DOS) of this structure are presented in Figs. 1(c) and 1(d) [25,30,31], revealing several  $E_F$  crossings of the bands with a dominant contribution from V 3d orbitals. This normal state electronic structure is compared with our static ARPES measurements of the 1T-VSe<sub>2</sub> dispersion in the CDW phase performed with synchrotron radiation over a photon energy range of 65–160 eV, as seen in Figs. 1(e) and 1(f). In the  $(k_{\parallel}, k_{\perp})$ -dependent photoemission intensity around high-symmetry points of the bulk BZ near  $E_F$  in Fig. 1(e), a strikingly high signal appears around  $\Gamma$  [25]. This is seen in Fig. 1(f) to emerge from a flat part of the dispersion that crosses  $E_F$  toward  $K$ . Monitoring the response of the system to an optical excitation in this direction thus provides access to excited carriers following the band and thereby the broadening of the Fermi-Dirac (FD) function caused by an elevated electronic temperature,  $T_e$ , resulting from thermalization of the carriers [32]. We do not find any clear manifestation of the CDW in the static ARPES intensity [8,25].

We now focus on TR-ARPES measurements performed along the selected  $k_{\parallel}$ -cut, as demonstrated in Fig. 2(a). The features are well-described by the overlaid DFT bands along  $M$ - $\Gamma$ - $K$  and closely resemble the synchrotron data in Fig. 1(f) with differences in intensity arising from the change of

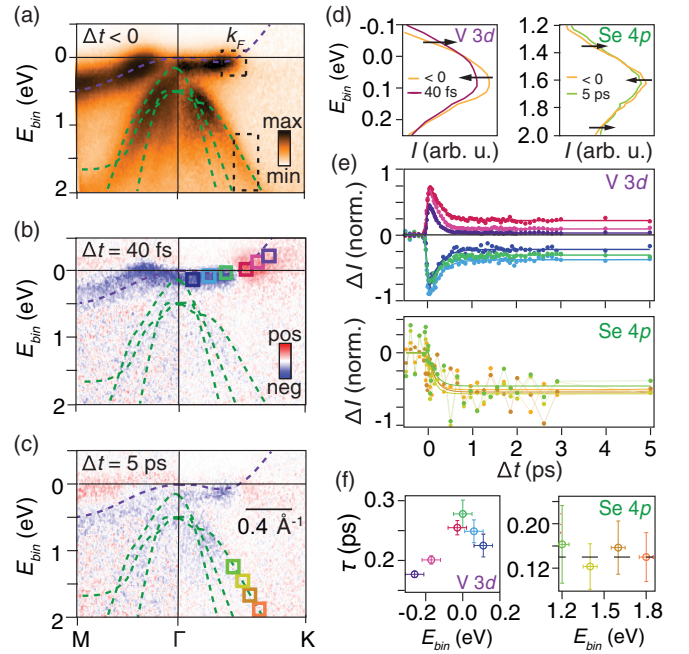


FIG. 2. (a) TR-ARPES intensity along  $M$ - $\Gamma$ - $K$  before optical excitation ( $\Delta t < 0$ ). (b),(c) Intensity difference between a spectrum obtained at the given time delay and the equilibrium spectrum in (a). The dashed lines are DFT bands, which encode V 3d (purple lines) and Se 4p (green lines) character. (d) EDCs integrated over the momentum range indicated in (a) by dashed boxes around the Fermi energy (left panel) and around the Se 4p bands (right panel). The arrows indicate the redistribution of intensity following photoexcitation. (e) Intensity difference integrated over the  $(E_{\text{bin}}, k_{\parallel})$ -regions demarcated by correspondingly colored boxes in (b),(c). The smooth curves are fits to an exponential. (f) Time constants for the exponential fits in (e). The markers have been colored according to the corresponding boxes in (b),(c) and the curves in (e). The dashed line in the right panel represents an average time constant.

photon energy and the different photoemission geometries [25]. Figures 2(b) and 2(c) present the intensity difference between an excited state spectrum at the given time delays,  $\Delta t$ , and the equilibrium spectrum in Fig. 2(a) following optical excitation. The red (blue) regions in Figs. 2(b) and 2(c) correspond to photoemission intensity gain (loss). Immediately after the excitation, at  $\Delta t = 40$  fs, the signal along  $\Gamma$ - $K$  exhibits a loss below  $E_F$  that is compensated for by a gain in the band above  $E_F$ , indicating the presence of excited holes and electrons. At  $\Delta t = 5$  ps, a significant intensity difference is still observable around the  $E_F$  crossing. As most clearly seen by the momentum-integrated energy distribution curves (EDCs) in Fig. 2(d), an additional loss (gain) of intensity is seen around the center (tail) of all the bands, indicating an overall broadening effect. The left panel in Fig. 2(d) presents EDCs around the Fermi wave vector,  $k_F$ , at equilibrium ( $t < 0$ ) and at the peak of excitation (40 fs), demonstrating the filling (depletion) of electrons above (below)  $E_F$ . The right panel in Fig. 2(d) shows EDCs for the Se 4p bands toward higher binding energy at a long delay (5 ps), exhibiting a significant broadening effect, similar to the corresponding intensity difference in Fig. 2(c). We emphasize that

we do not observe any rigid energy shifts in the EDCs, thereby ruling out a significant influence from extrinsic space-charge effects.

The detailed time-dependence of these signals is investigated by integrating the intensity difference within the  $(E_{\text{bin}}, k_{\parallel})$ -regions following the bands, as marked by colored boxes, in Figs. 2(b) and 2(c). The resulting  $\Delta I(t)$  curves are shown in Fig. 2(e). The upper panel presents the intensity changes in the V 3d states around  $E_F$ . A sharp transient, nearly symmetric for holes and electrons, is observed, followed by a brief relaxation period before the signal reaches a metastable situation that remains far from the equilibrium signal on the timescale we probe. In the lower panel, we inspect the time-dependence of the broadening of the Se 4p states. Interestingly, this effect grows after the excitation and settles at a fixed level without any sign of recovery for the probed time delays. Exponential function fits of the relaxation part in the V 3d states and the change of intensity in the Se 4p states provide the energy-dependence of the time constants shown in Fig. 2(f). In the V 3d states, the relaxation slows down toward the Fermi energy, reflecting the behavior expected for hot carriers that follow the FD distribution [27,33]. The states toward higher binding energies broaden on a timescale of around 150 fs, which is independent of the selected  $(E_{\text{bin}}, k_{\parallel})$ -window as seen in the right panel in Fig. 2(f).

The conventional analysis presented above is not sufficient to disentangle the contributions of the quasiparticle response and the hot carrier population to the intensity difference, it can merely identify their presence. To extract the full temporal evolution of the above parameters, we assume the proportional relation between the photoemission intensity,  $\mathcal{I}$ , and the product  $\mathcal{A}(E_{\text{bin}}, k_{\parallel})f_{\text{FD}}(E, T_e)$ , where  $T_e$  enters via the FD distribution,  $f_{\text{FD}}$ . The spectral function is described by  $\mathcal{A}(E_{\text{bin}}, k_{\parallel}) = \pi^{-1} |\Sigma''| / \{ [E_{\text{bin}} - \epsilon(k_{\parallel}) - \Sigma']^2 + \Sigma''^2 \}$ , where  $\epsilon(k_{\parallel})$  is the bare dispersion,  $\Sigma'$  is the real part, and  $\Sigma''$  is the imaginary part of the electronic self-energy. This framework is commonly used to analyze static ARPES data [32,34–36], but here we explore its utility to describe quasithermal TR-ARPES spectra. To simulate the measured 2D image of  $\mathcal{I}(E_{\text{bin}}, k_{\parallel})$ , we use the DFT bands overlaid in Figs. 2(a)–2(c) in place of the bare dispersion  $\epsilon(k_{\parallel})$ . Since no time-dependent shifts in the band positions are observed in the data, we approximate  $\Sigma'$  as a time-independent constant. The time-dependent broadening effects are encoded in  $\Sigma''$ , which is taken as independent of energy and momentum within the V 3d and Se 4p states, justified by the analysis discussed in connection with Figs. 2(e) and 2(f). By fitting  $T_e$  and  $\Sigma''$  in the simulated intensity to the measured ARPES intensity at each time delay, we are able to obtain an excellent description of the data, as seen by comparing Figs. 3(a) and 3(b), as well as the example EDCs in Fig. 3(c). The observation of a FD distribution at all time delays is consistent with a quasithermal equilibrium, evidencing that the phenomenological description of the ARPES intensity can be successfully extended to out-of-equilibrium ARPES experiments with quasithermalized hot electrons. A maximum electronic temperature of  $(737 \pm 30)$  K is observed immediately after excitation, leading to a significant redistribution of carriers in the V 3d states, as seen via the change of width of the FD function in Fig. 3(d).

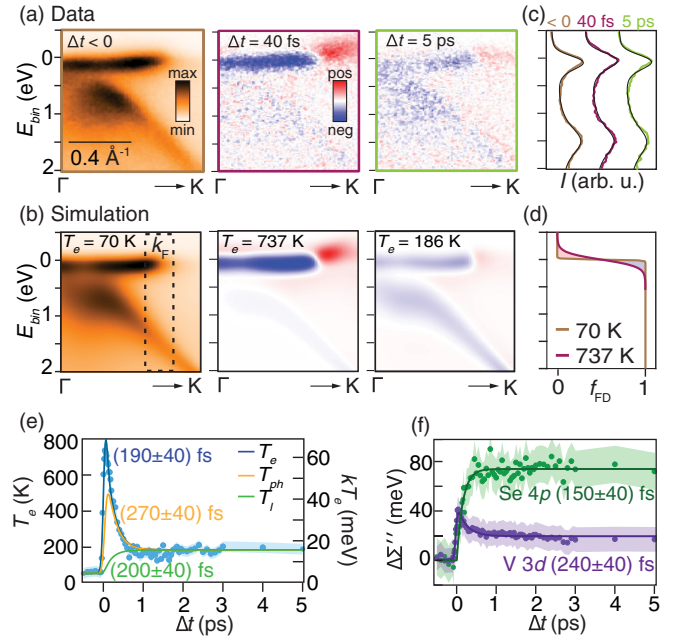


FIG. 3. (a) ARPES intensity in equilibrium (left panel) and intensity difference at  $\Delta t = 40$  fs (middle panel) and  $\Delta t = 5$  ps (right panel) along  $\Gamma$ -K. (b) Simulations of the ARPES intensity and the resulting intensity difference and electronic temperature,  $T_e$ , from fits of the data displayed in the same column in (a). (c) Measured (colored curves) and simulated (smooth black curves) EDCs integrated over the momentum range indicated by the black dashed box in the left panel in (b) for the given time delays. (d) Fermi-Dirac distributions at the extreme electronic temperatures. (e) Temporal evolution of  $T_e$  and the temperature of strongly coupled modes,  $T_{\text{ph}}$ , and remaining lattice,  $T_l$ , determined via a three-temperature model [25]. Markers correspond to  $T_e$  values obtained from the intensity simulations. The time constants are given for the initial relaxations of  $T_e$  and  $T_{\text{ph}}$  and heating of  $T_l$ . (f) Time-dependent change of the imaginary part of the electronic self-energy for the V 3d (purple markers) and Se 4p (green markers) states determined from the spectral function fits. Smooth curves are fits to functions with the given time constants for the exponential components. The shaded regions in (e),(f) indicate the error associated with extracted values.

Figure 3(e) presents the time-dependent change of  $T_e$ . Following a steplike response to the optical excitation, an initial relaxation on a timescale of  $(190 \pm 40)$  fs occurs before a new thermal equilibrium with an elevated  $T_e$  is reached. The initial fast relaxation period is explained by incoherent coupling between the hot electrons and phonons. Using a three-temperature model (3TM) incorporating a fraction of strongly coupled Einstein modes and an anharmonic decay of these modes involving the remaining lattice provides an estimate of the temporal evolution of the strongly coupled phonon temperature,  $T_{\text{ph}}$ , and the lattice temperature,  $T_l$ , as shown in Fig. 3(e) [25–27,37–40]. The fraction of Einstein modes is centered at an energy of 21 meV, which we justify below. The lattice reaches a temperature of  $(182 \pm 30)$  K on a timescale of  $(200 \pm 40)$  fs, such that the metastable thermal equilibrium between all three temperatures occurs above  $T_c = 110$  K.

The temporal behavior of the self-energy for the V 3d states in Fig. 3(f) resembles closely that of  $T_e$ , reflecting the

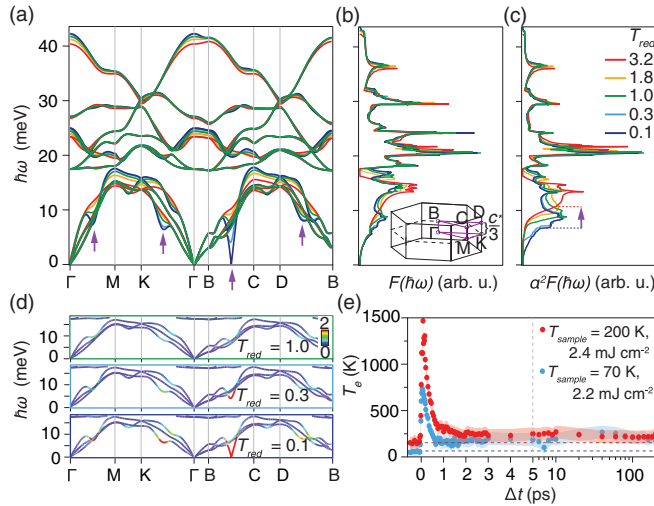


FIG. 4. (a)–(c) Density functional perturbation theory results for (a) phonon dispersion, (b) phonon DOS, and (c) Eliashberg function. The inset in (b) displays the hexagonal BZ with the momentum path in (a) indicated by purple lines. The colors of the curves correspond to the reduced electronic temperatures,  $T_{red} = (T_e - T_c^*)/T_c^*$ , stated in (c). Purple arrows in (a) and (c) indicate phonon energies that depend significantly on  $T_{red}$ . (d) Acoustic phonon dispersion with EPC strength encoded by the color scale at the given values of  $T_{red}$ . (e) Temporal evolution of  $T_e$  measured by TR-ARPES with the sample kept at 70 K (blue markers) and 200 K (red markers) at the given pump laser fluence. Note the logarithmic scale after  $\Delta t = 5$  ps. The shaded area indicates the error bar associated with the extraction of  $T_e$ .

changing number of available scattering channels as a result of initial depopulation and subsequent incomplete repopulation of these electronic states. The distinct time-dependent evolution of  $\Sigma''$  for the Se  $4p$  states at higher binding energies, seen in Fig. 3(f), is more striking since the population of these states remains fixed. Interestingly, the timescale for self-energy increase is correlated with the heating of the lattice in Fig. 3(e). The enhancement of  $\Sigma''$  likely originates from the opening of new scattering channels for the decay of the photohole involving absorption of the excited hot phonons.

We explore how the electron-phonon interactions are altered through the excitation and relaxation processes by calculating the phonon dispersion and associated mode-resolved EPC using density functional perturbation theory (DFPT) [25,41–47]. We note that the critical temperature obtained from the calculations,  $T_c^*$ , overestimates the experimentally observed value [48,49]. To ensure that we can reproducibly describe the normal phase of  $1T$ -VSe $_2$ , we perform a set of calculations at a range of reduced electronic temperatures,  $T_{red} = (T_e - T_c^*)/T_c^*$ . The obtained phonon dispersion and associated DOS are shown in Figs. 4(a) and 4(b), reflecting the impact of electronic screening on the lattice vibrations [48,50,51]. The selected path in  $\mathbf{q}$ -space is indicated by the BZ sketch in Fig. 4(b). At temperatures close to  $T_c^*$ , the phonon dispersion contains a number of soft acoustic modes, seen as cusps in Fig. 4(a). Around the CDW wave vector, the soft mode frequency becomes imaginary below  $T_c^*$ , creating an instability toward lattice deformation [25]. The EPC-weighted phonon DOS given by the Eliashberg function,

$\alpha^2F$ , reveals a sharp peak from the optical branches at 21 meV in Fig. 4(c). The combination of a high phonon energy and a large EPC strength leads to a strong weight of these optical modes in the energy transfer rate equations that form the basis for the 3TM model discussed in connection with Fig. 3(e) [37]. As  $T_{red}$  increases, the soft modes disappear, and the low-energy peaks in  $\alpha^2F$  shift to higher energies [see the purple arrows in Figs. 4(a) and 4(c)], consistent with the calculated band-resolved phonon dispersion and EPC at selected  $T_{red}$  in Fig. 4(d). The phase space of soft modes and the coupling to these modes thus weakens with increasing  $T_e$ , removing possible efficient cooling channels for the hot carriers.

Reconciling our 3TM model with the DFPT calculations, we arrive at a complete picture of electron-phonon dynamics in  $1T$ -VSe $_2$ : For the initial decay of  $T_e$ , the energy loss to optical phonons dominates. However, at lower temperatures where  $kT_e < 21$  meV, the decay of electrons by emission of an optical phonon of this energy becomes inefficient. At the same time, the CDW phase has been removed together with many of the efficient low-energy acoustic phonon channels, resulting in  $T_e$  becoming stuck. The removal of the acoustic phonon scattering channels justifies the choice of not including an electron-acoustic phonon term in our 3TM model.

Finally, we consider the time-dependence of  $T_e$  up to 200 ps after the optical excitation for the sample held at temperatures below and above  $T_c$ , as shown in Fig. 4(e). For the sample above  $T_c$  (200 K), the maximum in the electronic temperature is higher than for the sample below  $T_c$  (70 K), which we ascribe to a higher laser fluence used in the former case. Overall, however, we observe a very similar time-dependent response in the two situations, with a single rapid decay of  $T_e$  followed by a long-lived plateau. A metastable state develops regardless of the initial state of the sample at equilibrium. Furthermore, the temperature evolution of the soft phonon mode is characteristic of a second-order phase transition, precluding an energy barrier between the normal state and the CDW [25,52,53]. Instead, the optical excitation establishes a new quasiequilibrium state with a phonon dispersion locked by the elevated  $T_e$ , which persists for at least hundreds of picoseconds.

Our results demonstrate that a femtosecond optical excitation of  $1T$ -VSe $_2$  leads to a rapidly thermalized hot carrier distribution, which cools on a  $(190 \pm 40)$  fs timescale via incoherent electron-phonon interactions that in turn heat the lattice above the CDW transition temperature. The hot carriers dynamically affect the low-energy soft phonon spectrum and EPC strength, leaving the system in a quasiequilibrium. Such long-lived light-induced states could play a significant role for the dynamics in other CDW materials where the presence of hot carriers leads to the quenching of the soft phonon modes that participate in stabilizing the CDW state.

The research data supporting this publication can be accessed at [54].

We thank Phil Rice, Alistair Cox, and David Rose for technical support during the Artemis beamtime. We gratefully acknowledge funding from VILLUM FONDEN through the Young Investigator Program (Grant. No. 15375) and the

Centre of Excellence for Dirac Materials (Grant. No. 11744), the Danish Council for Independent Research, Natural Sciences under the Sapere Aude program (Grants No. DFF-9064-00057B and No. DFF-6108-00409), and the Aarhus University Research Foundation. This work is also supported by National Research Foundation (NRF) grants funded by the Korean government (No. NRF-2020R1A2C200373211 and No. 2019K1A3A7A09033389) and by the International Max Planck Research School for Chemistry and Physics of Quantum Materials (IMPRS-CPQM). The authors also ac-

knowledge The Royal Society and The Leverhulme Trust. R.S. acknowledges financial support provided by the Ministry of Science and Technology in Taiwan under Project No. MOST-108-2112-M-001-049-MY2 & MOST 109-2124-M-002-001 and Sinica funded i-MATE financial Support AS-iMATE-109-13. Access to the Artemis Facility was funded by STFC. The Advanced Light Source is supported by the Director, Office of Science, Office of Basic Energy Sciences, of the U.S. Department of Energy under Contract No. DE-AC02-05CH11231.

- [1] C. F. van Bruggen and C. Haas, *Solid State Commun.* **20**, 251 (1976).
- [2] K. Tsutsumi, *Phys. Rev. B* **26**, 5756 (1982).
- [3] D. J. Eaglesham, R. L. Withers, and D. M. Bird, *J. Phys. C* **19**, 359 (1986).
- [4] J. Henke, F. Flicker, J. Laverock, and J. van Wezel, *Sci. Post Phys.* **9**, 56 (2020).
- [5] W. Jolie, T. Knispel, N. Ehlen, K. Nikonov, C. Busse, A. Grüneis, and T. Michely, *Phys. Rev. B* **99**, 115417 (2019).
- [6] K. Terashima, T. Sato, H. Komatsu, T. Takahashi, N. Maeda, and K. Hayashi, *Phys. Rev. B* **68**, 155108 (2003).
- [7] T. Sato, K. Terashima, S. Souma, H. Matsui, T. Takahashi, H. Yang, S. Wang, H. Ding, N. Maeda, and K. Hayashi, *J. Phys. Soc. Jpn.* **73**, 3331 (2004).
- [8] V. N. Strocov, M. Shi, M. Kobayashi, C. Monney, X. Wang, J. Krempasky, T. Schmitt, L. Patthey, H. Berger, and P. Blaha, *Phys. Rev. Lett.* **109**, 086401 (2012).
- [9] Á. Pásztor, A. Scarfato, C. Barreteau, E. Giannini, and C. Renner, *2D Mater.* **4**, 41005 (2017).
- [10] G. Duvjir, B. K. Choi, I. Jang, S. Ulstrup, S. Kang, T. T. Ly, S. Kim, Y. H. Choi, C. Jozwiak, A. Bostwick *et al.*, *Nano Lett.* **18**, 5432 (2018).
- [11] J. Feng, D. Biswas, A. Rajan, M. D. Watson, F. Mazzola, O. J. Clark, K. Underwood, I. Marković, M. McLaren, A. Hunter *et al.*, *Nano Lett.* **18**, 4493 (2018).
- [12] P. Chen, W. W. Pai, Y.-H. Chan, V. Madhavan, M. Y. Chou, S.-K. Mo, A.-V. Fedorov, and T.-C. Chiang, *Phys. Rev. Lett.* **121**, 196402 (2018).
- [13] J. Feng, R. A. Susilo, B. Lin, W. Deng, Y. Wang, B. Li, K. Jiang, Z. Chen, X. Xing, Z. Shi *et al.*, *Adv. Electron. Mater.* **6**, 1901427 (2020).
- [14] S. Sahoo, U. Dutta, L. Harnagea, A. K. Sood, and S. Karmakar, *Phys. Rev. B* **101**, 014514 (2020).
- [15] D. Zhang, J. Ha, H. Baek, Y.-H. Chan, F. D. Natterer, A. F. Myers, J. D. Schumacher, W. G. Cullen, A. V. Davydov, Y. Kuk *et al.*, *Phys. Rev. Mater.* **1**, 024005 (2017).
- [16] J. G. Si, W. J. Lu, H. Y. Wu, H. Y. Lv, X. Liang, Q. J. Li, and Y. P. Sun, *Phys. Rev. B* **101**, 235405 (2020).
- [17] D. M. Kennes, E. Y. Wilner, D. R. Reichman, and A. J. Millis, *Nat. Phys.* **13**, 479 (2017).
- [18] M. A. Sentef, *Phys. Rev. B* **95**, 205111 (2017).
- [19] E. Pomarico, M. Mitrano, H. Bromberger, M. A. Sentef, A. Al-Temimy, C. Coletti, A. Stöhr, S. Link, U. Starke, C. Cacho *et al.*, *Phys. Rev. B* **95**, 024304 (2017).
- [20] L. Perfetti, P. A. Loukakos, M. Lisowski, U. Bovensiepen, H. Berger, S. Biermann, P. S. Cornaglia, A. Georges, and M. Wolf, *Phys. Rev. Lett.* **97**, 067402 (2006).
- [21] T. Rohwer, S. Hellmann, M. Wiesenmayer, C. Sohrt, A. Stange, B. Slomski, A. Carr, Y. Liu, L. M. Avila, M. Källäne *et al.*, *Nature (London)* **471**, 490 (2011).
- [22] J. C. Petersen, S. Kaiser, N. Dean, A. Simoncig, H. Y. Liu, A. L. Cavalieri, C. Cacho, I. C. E. Turcu, E. Springate, F. Frassetto *et al.*, *Phys. Rev. Lett.* **107**, 177402 (2011).
- [23] S. Hellmann, T. Rohwer, M. Källäne, K. Hanff, C. Sohrt, A. Stange, A. Carr, M. M. Murnane, H. C. Kapteyn, L. Kipp *et al.*, *Nat. Commun.* **3**, 1069 (2012).
- [24] C. Monney, M. Puppini, C. W. Nicholson, M. Hoesch, R. T. Chapman, E. Springate, H. Berger, A. Magrez, C. Cacho, R. Ernstorfer *et al.*, *Phys. Rev. B* **94**, 165165 (2016).
- [25] See the supplemental material at <http://link.aps.org/supplemental/10.1103/PhysRevB.103.L241108> for experimental details on the photoemission measurements, for a complete description of the spectral function simulations, for the three-temperature model rate equations, and for details on the electronic structure calculations and the density functional perturbation theory applied for the phonon computations.
- [26] L. Perfetti, P. A. Loukakos, M. Lisowski, U. Bovensiepen, H. Eisaki, and M. Wolf, *Phys. Rev. Lett.* **99**, 197001 (2007).
- [27] J. C. Johannsen, S. Ulstrup, F. Cilento, A. Crepaldi, M. Zacchigna, C. Cacho, I. C. Edmond Turcu, E. Springate, F. Fromm, C. Raidel, T. Seyller, F. Parmigiani, M. Grioni, and P. Hofmann, *Phys. Rev. Lett.* **111**, 027403 (2013).
- [28] C. J. Sayers, L. S. Farrar, S. J. Bending, M. Cattelan, A. J. H. Jones, N. A. Fox, G. Kociok-Köhn, K. Koshmak, J. Laverock, L. Pasquali *et al.*, *Phys. Rev. Mater.* **4**, 025002 (2020).
- [29] A. Feroze, H. R. Na, Y. C. Park, J.-H. Jun, M.-H. Jung, J.-H. Lee, J.-H. Kim, M.-J. Seong, S. Hong, S.-H. Chun *et al.*, *Cryst. Growth Des.* **20**, 2860 (2020).
- [30] P. Blaha, K. Schwarz, F. Tran, R. Laskowski, G. K. H. Madsen, and L. D. Marks, *J. Chem. Phys.* **152**, 074101 (2020).
- [31] J. P. Perdew, K. Burke, and M. Ernzerhof, *Phys. Rev. Lett.* **77**, 3865 (1996).
- [32] S. Ulstrup, J. C. Johannsen, M. Grioni, and P. Hofmann, *Rev. Sci. Instrum.* **85**, 13907 (2014).
- [33] A. Crepaldi, B. Ressel, F. Cilento, M. Zacchigna, C. Grazioli, H. Berger, P. Bugnon, K. Kern, M. Grioni, and F. Parmigiani, *Phys. Rev. B* **86**, 205133 (2012).
- [34] I. A. Nechaev, M. F. Jensen, E. D. L. Rienks, V. M. Silkin, P. M. Echenique, E. V. Chulkov, and P. Hofmann, *Phys. Rev. B* **80**, 113402 (2009).

- [35] F. Andreatta, H. Rostami, A. G. Cabo, M. Bianchi, C. E. Sanders, D. Biswas, C. Cacho, A. J. H. Jones, R. T. Chapman, E. Springate, P. D. C. King, J. A. Miwa, A. Balatsky, S. Ulstrup, and P. Hofmann, *Phys. Rev. B* **99**, 165421 (2019).
- [36] D. Biswas, A. J. H. Jones, P. Majchrzak, B. K. Choi, T.-H. Lee, K. Volckaert, J. Feng, I. Marković, F. Andreatta, C.-J. Kang *et al.*, *Nano Lett.* **21**, 1968 (2021).
- [37] P. B. Allen, *Phys. Rev. Lett.* **59**, 1460 (1987).
- [38] T. Kampfrath, L. Perfetti, F. Schapper, C. Frischkorn, and M. Wolf, *Phys. Rev. Lett.* **95**, 187403 (2005).
- [39] S. Dal Conte, C. Giannetti, G. Coslovich, F. Cilento, D. Bossini, T. Abebaw, F. Banfi, G. Ferrini, H. Eisaki, M. Greven *et al.*, *Science* **335**, 1600 (2012).
- [40] C. S. Yadav and A. K. Rastogi, *Solid State Commun.* **150**, 648 (2010).
- [41] A. Migdal, *J. Exptl. Theoret. Phys. (U.S.S.R.)* **34**, 1438 (1958) [*Sov. Phys. JETP* **7**, 996 (1958)].
- [42] G. Eliashberg, *J. Exptl. Theoret. Phys. (U.S.S.R.)* **38**, 966 (1960) [*Sov. Phys. JETP* **11**, 696 (1960)].
- [43] P. Giannozzi, S. Baroni, N. Bonini, M. Calandra, R. Car, C. Cavazzoni, D. Ceresoli, G. L. Chiarotti, M. Cococcioni, I. Dabo *et al.*, *J. Phys.: Condens. Matter* **21**, 395502 (2009).
- [44] D. Vanderbilt, *Phys. Rev. B* **41**, 7892 (1990).
- [45] S. Grimme, *J. Comput. Chem.* **27**, 1787 (2006).
- [46] M. Bayard and M. J. Sienko, *J. Solid State Chem.* **19**, 325 (1976).
- [47] N. Marzari, D. Vanderbilt, A. De Vita, and M. C. Payne, *Phys. Rev. Lett.* **82**, 3296 (1999).
- [48] D. L. Duong, M. Burghard, and J. C. Schön, *Phys. Rev. B* **92**, 245131 (2015).
- [49] R. Bianco, L. Monacelli, M. Calandra, F. Mauri, and I. Errea, *Phys. Rev. Lett.* **125**, 106101 (2020).
- [50] W. Kohn, *Phys. Rev. Lett.* **2**, 393 (1959).
- [51] S. K. Chan and V. Heine, *J. Phys. F* **3**, 795 (1973).
- [52] S. Wall, B. Krenzer, S. Wippermann, S. Sanna, F. Klasing, A. Hanisch-Blicharski, M. Kammler, W. G. Schmidt, and M. Horn-von Hoegen, *Phys. Rev. Lett.* **109**, 186101 (2012).
- [53] J. Diego, A. H. Said, S. K. Mahatha, R. Bianco, L. Monacelli, M. Calandra, F. Mauri, K. Rossnagel, I. Errea, and S. Blanco-Canosa, *Nat. Commun.* **12**, 598 (2021).
- [54] P. Majchrzak, S. Pakdel, D. Biswas, A. J. H. Jones, K. Volckaert, I. Markovic, F. Andreatta, R. Sankar, C. Jozwiak, E. Rotenberg, A. Bostwick, C. E. Sanders, Y. Zhang, G. Karras, R. T. Chapman, A. Wyatt, E. Springate, J. A. Miwa, P. Hofmann, P. D. C. King, N. Lanatá, Y. J. Chang and S. Ulstrup, dataset for Switching of the electron-phonon interaction in 1T-VSe<sub>2</sub> assisted by hot carriers, University of St Andrews Research Portal, 2021, doi: [10.17630/8181a2eb-3fa6-4be1-8b07-dc52a9383fb3](https://doi.org/10.17630/8181a2eb-3fa6-4be1-8b07-dc52a9383fb3).